ACSNANO

www.acsnano.org

ARTICLE

Tunable Band-Edge Potentials and Charge Storage in Colloidal Tin-Doped Indium Oxide (ITO) Nanocrystals

Jose J. Araujo, Carl K. Brozek, Hongbin Liu, Anna Merkulova, Xiaosong Li, and Daniel R. Gamelin*

Cite This: *ACS Nano* 2021, 15, 14116−14124

Read Online

ACCESS | Metrics & More | Article Recommendations | Supporting Information

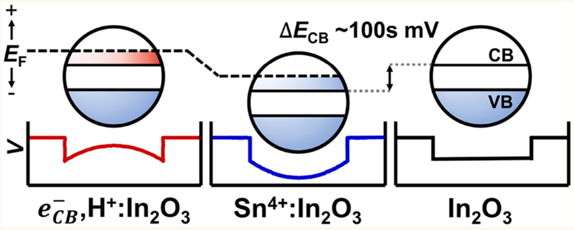

ABSTRACT: Degenerately doped metal-oxide nanocrystals (NCs) show localized surface plasmon resonances (LSPRs) that are tunable via their tunable excess charge-carrier densities. Modulation of excess charge carriers has also been used to control magnetism in colloidal doped metal-oxide NCs. The addition of excess delocalized conduction-band (CB) electrons can be achieved through aliovalent doping or by postsynthetic techniques such as electrochemistry or photodoping. Here, we examine the influence of charge-compensating aliovalent dopants on the potentials of excess CB electrons in free-standing colloidal degenerately doped oxide NCs, both experimentally and through modeling. Taking Sn^{4+}:In_2O_3 (ITO) NCs as a model system, we use spectroelectrochemical techniques to examine differences between aliovalent doping and photodoping. We demonstrate that whereas photodoping introduces excess CB electrons by *raising* the Fermi level relative to the CB edge, aliovalent impurity substitution introduces excess CB electrons by *stabilizing* the CB edge relative to an externally defined Fermi level. Significant differences are thus observed electrochemically between spectroscopically similar delocalized CB electrons compensated by aliovalent dopants and those compensated by surface cations (e.g., protons) during photodoping. Theoretical modeling illustrates the very different potentials that arise from charge compensation via aliovalent substitution and surface charge compensation. Spectroelectrochemical titrations allow the ITO NC band-edge stabilization as a function of Sn^{4+} doping to be quantified. Extremely large capacitances are observed in both In_2O_3 and ITO NCs, making these NCs attractive for reversible charge-storage applications.

KEYWORDS: *metal-oxide nanocrystals, n-doping, photodoping, redox potentials, charge compensation, band engineering, impurity doping*

Degenerately doped semiconductor nanocrystals (NCs) have attracted considerable attention for their tunable electronic, optoelectronic, photophysical, and spin-based properties.[1−15] Doped metal-oxide NCs such as Al^{3+}:ZnO (AZO),[16,17] Sn^{4+}:In_2O_3 (ITO),[18−20] and In^{3+}:CdO (ICO),[21,22] have become particularly attractive for their tunable localized surface plasmon resonances (LSPRs).[1,2,11,23] Both the LSPR intensity and its energy can be tuned broadly in this class of materials because of their tunable charge-carrier densities, accessed variously through aliovalent doping,[16−18,24] electrochemical charging,[25,26] photodoping,[5,11,18,27] and redox chemistry.[28−30] A thorough fundamental understanding of the properties of charge carriers introduced through these various methods is necessary for implementation of next-generation technologies based on degenerately doped semiconductor NCs.

Charge compensation plays a major role in determining the properties of excess charge carriers in semiconductor NCs. For example, the redox potentials of excess electrons introduced via photodoping or molecular electron transfer are very sensitive to changes in the steric bulk of the charge-compensating ion,[31,32] and electrostatic modeling describes a strong dependence of carrier potentials on the counterion's distance from the NC surface.[33,34] Recently, spectroelectrochemical measurements revealed a ∼500 mV difference between the stabilization of valence-band (VB) holes compensated by lattice vacancies in $Cu_{2-x}S$ NCs compared to similar holes stabilized by surface anions.[35] Similarly, conduction-band (CB) electrons compensated by aliovalent dopants in AZO and ITO NCs were found to be strikingly less reducing than spectroscopically comparable electrons introduced via photodoping and compensated by surface protons.[16,18] Density functional theory (DFT)

Received: June 1, 2021
Accepted: August 10, 2021
Published: August 13, 2021

https://doi.org/10.1021/acsnano.1c04660
ACS Nano 2021, 15, 14116−14124

calculations show very large stabilization of CB orbitals by substitutional Al^{3+} in AZO NCs,[36] but the band-edge potentials of free-standing aliovalently doped metal-oxide NCs have not been measured experimentally.

Here, we report spectroelectrochemical measurements of degenerately doped metal-oxide NCs with different aliovalent doping levels and with and without additional photodoping. ITO NCs were selected as a model system for this study because of their highly controllable synthesis. Titration of CB electrons from photodoped ITO NCs provides a direct experimental measure of NC electron densities stemming from both photodoping and aliovalent doping, and additionally shows that aliovalent dopants dramatically stabilize the NC CB edge (i.e., lower its energy), as opposed to raising the Fermi level. These experimental results are supplemented by theoretical analysis using the Charged Sphere model,[33,34] which shows much greater electrostatic stabilization of CB electrons in the NC cores when their charge-compensating counterions are embedded within the NC lattice as aliovalent dopants than when they are located at the NC surfaces. *In situ* potentiometric data collected during titration further reveal very large capacitance values for these In_2O_3-based NCs that may prove attractive for reversible charge-storage applications involving colloidal nanomaterials.

RESULTS AND DISCUSSION

In_2O_3 NCs were synthesized with varying Sn^{4+} content following literature procedures.[19,24] Figure 1a shows absorption spectra of In_2O_3 and ITO NCs of varying Sn^{4+} concentration (cation %). An intense localized surface plasmon resonance (LSPR) is observed in the near-infrared (NIR) of all ITO NC samples, shifting to higher energy as more Sn^{4+} is incorporated, consistent with electronic doping from the addition of Sn^{4+}. A small amount of NIR absorption is also observed in the undoped In_2O_3 NCs, potentially from free electrons associated with native oxygen vacancies.[37,38] TEM analysis (Figure 1b−e) shows that these NCs range between 12 and 15 nm in diameter (see Supporting Information (SI) for size distribution analysis). As seen in these images, the introduction of Sn^{4+} influences the NC faceting.

Figure 2 summarizes absorption data from a representative spectroelectrochemical potentiometry experiment performed on these ITO NCs. For these measurements, $d = 14.1$ nm ITO NCs containing 1.9% Sn^{4+} were used. The sample was first photodoped until the NIR absorption stopped increasing and V_{OC} (*vide infra*) stopped changing. Then, the solution was titrated with aliquots of $FcBF_4$ in 0.1 M $TBAPF_6$/THF. The LSPR absorption decreased as $FcBF_4$ was added, until the as-prepared spectrum was recovered (Figure 2a), consistent with removal of the CB electrons introduced by photodoping ($e^-_{CB,\ photo}$). Further additions of $FcBF_4$ resulted in a further decrease of the plasmon absorption, indicating removal of some of the electrons compensated by the aliovalent dopants ($e^-_{CB,\ alio}$). Eventually, the spectra stopped changing with the addition of more $FcBF_4$, indicating that no more $e^-_{CB,\ alio}$ can be removed from the NCs with this oxidant. By plotting the ratio of the NIR absorbance at 1300 nm (similar results are obtained for other monitoring wavelengths) to the absorbance of the as-prepared solution at the same wavelength (i.e., A/A_0) against equivalents of $FcBF_4$ added per NC (Figure 2b), the data can be analyzed quantitatively.

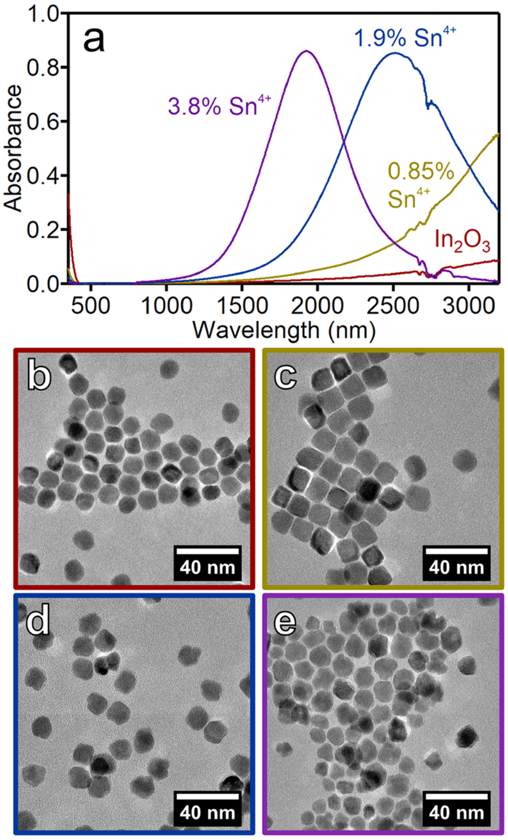

Figure 1. (a) Room-temperature absorption spectra of $d = 13.1$ nm In_2O_3 (red), $d = 13.4$ nm 0.85% ITO (gold), $d = 14.1$ nm 1.9% ITO (blue), and $d = 12.6$ nm 3.8% ITO (purple) nanocrystals. The spectra were measured using tetrachloroethylene as the solvent. Panels (b), (c), (d), and (e) show TEM micrographs of the undoped In_2O_3, 0.85%, 1.9%, and 3.8% Sn^{4+}-doped In_2O_3 (ITO) NCs, respectively.

As shown in Figure 2b, A/A_0 decreases linearly with the addition of $FcBF_4$ for values of $A/A_0 > 1$, consistent with removal of one electron per equivalent of $FcBF_4$ added. The dashed blue line is a linear fit to this portion of the data. The intersection of this fitted line with $A/A_0 = 1$ indicates the average number of CB electrons per NC added via photodoping ($\langle n_{photo} \rangle \sim 232$), and extrapolation of this line to $A/A_0 = 0$ yields the total number of CB electrons per NC ($\langle n_{total} \rangle \sim 637$) at maximum photodoping. Subtracting $\langle n_{photo} \rangle$ from $\langle n_{total} \rangle$ gives the average number of CB electrons in the as-prepared ITO NCs ($\langle n_{alio} \rangle \sim 405$). ICP analysis shows that this 1.9% ITO NC sample contains ~880 Sn^{4+} cations per NC on average, but the titration data indicate only ~405 excess CB electrons per NC, showing that only 46% of all tin dopants are accompanied by excess CB electrons. Similarly, the 0.85% and 3.8% ITO samples show only 28% and 43% dopant activation, respectively, with no evident correlation between dopant activation percentages and other properties such as NC diameter, surface area, absolute doping level, or Fermi levels (*vide infra*). This result is reminiscent of the observation that only 5% of Al^{3+} dopants in AZO NCs lead to CB electrons;[16] the remaining aliovalent dopants are charge-compensated locally, for example, by other defects or surface nonstoichiometries.

The titration data in Figure 2b are no longer linear at $A/A_0 < 1$, and they plateau at $A/A_0 \approx 0.68$. This result indicates that ~32% of $\langle n_{alio} \rangle$ (~130 e^-/NC) can be removed by the oxidant, $FcBF_4$. The same analysis was performed on photodoped

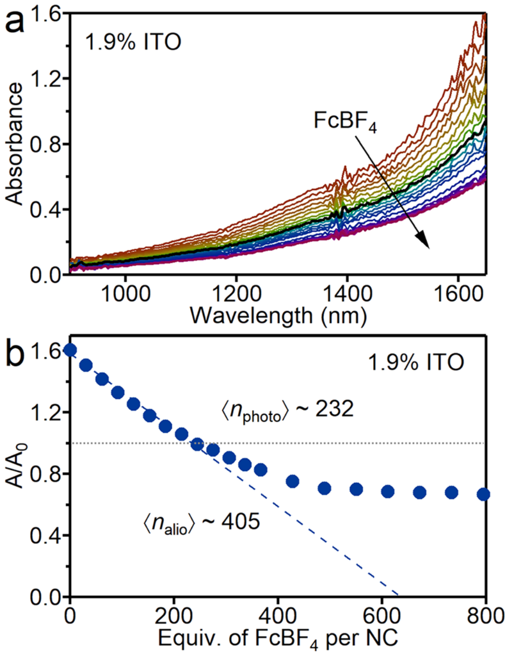

Figure 2. (a) Absorption spectra of a solution of maximally photodoped d = 14.1 nm ITO NCs containing 1.9% Sn^{4+}, collected at various stages during oxidative titration with $FcBF_4$. The NCs were suspended in 0.1 M $TBAPF_6$/THF. The arrow shows the direction of increasing oxidative equivalents. The black spectrum is the absorption of the as-prepared solution. (b) The ratio of the absorbance at 1300 nm to the absorbance of the as-prepared solution at the same wavelength (A/A_0), plotted against equivalents of $FcBF_4$ added to the maximally photodoped NCs from panel (a). The gray dotted line at A/A_0 = 1 represents the absorption of the as-prepared solution. The dashed blue line is a fit to the data for values of A/A_0 greater than 1 and is extrapolated to A/A_0 = 0.

In_2O_3, 0.85% ITO, and 3.8% ITO NCs (SI Figures S2−S4). For all of these NCs, the average additional CB electron density introduced by maximum photodoping is $\langle N_{photo}\rangle \sim 1.5 \times 10^{20}$ cm^{-3}, independent of Sn^{4+} concentration (SI Figure S5), consistent with our previous observations for photodoped ITO NCs.[18]

Figure 3 summarizes potentiometric titration data for the entire series of NCs shown in Figure 1. The data are plotted as Fermi level (E_F, in V vs $Fc^{+/0}$) vs equivalents of $FcBF_4$ added per NC, starting from the maximally photodoped NCs in each case. SI Figure S6 shows the same potentiometric data recast as E_F vs equivalents of $FcBF_4$ per NC surface area. These plots show E_F becoming progressively more positive as $FcBF_4$ is added to the solution of photodoped NCs. This result demonstrates that photodoping raises the Fermi level relative to that of the as-prepared NCs. At some number of equivalents, E_F drops sharply, indicating that the titration equivalence point has been reached. Beyond the equivalence point, E_F approaches the formal potential of $Fc^{+/0}$ (0 V). These data reflect a redox equilibrium between the NCs and the titrant.

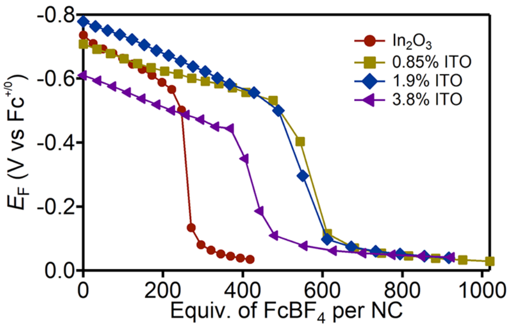

Figure 3. Potentiometric titration data for d = 13.1 nm In_2O_3 (red circles), d = 13.4 nm 0.85% ITO (gold squares), d = 14.1 nm 1.9% ITO (blue diamonds), and d = 12.6 nm 3.8% ITO (purple triangles) NCs. The Fermi level (E_F, in V vs $Fc^{+/0}$) is plotted against equivalents of $FcBF_4$ per NC added to solutions of maximally photodoped NCs in 0.1 M $TBAPF_6$/THF.

Table 1 summarizes the potentiometric data from Figure 3. The slopes of the potentiometric titration curves are given as mV/equiv and provide a measure of the NC redox capacitance (C_r) according to $1/C_r = \Delta V/\Delta Q = m/e$, where m is the titration slope (in V/equiv) and e is the elementary charge. These experimental capacitance values are compared with calculated double layer capacitance values given by eq 1, where A is the NC surface area, ϵ_0 is the vacuum permittivity (8.85×10^{-12} F m^{-1}), $\epsilon = 9$ is the dielectric of 0.1 M $TBAPF_6$/THF, R is the NC radius, and t is the double-layer thickness. The data are reproduced reasonably well using a best-fit value of $t \sim 1.4$ Å. This result is similar to typical surface O−H bond lengths (∼1.0 Å), suggesting that the majority of titrated electrons are charge-compensated directly at the NC surfaces, for example by surface protonation during photodoping. The differences between C_r and C_{dl} in Table 1 are again not obviously correlated with other factors, and are attributed to sample-dependent deviations from the idealized spherical double-layer model. The effective t deduced from this model represents all interactions simultaneously and obscures microscopic subtleties such as surface heterogeneity, patchy charge distributions, or partial proton intercalation. We note that the chemically reasonable value of t and the observation that electrons added via photodoping have far more negative potentials than those added by Sn^{4+} doping (even though intercalated protons are electrostatically equivalent to aliovalent dopants) both point against significant proton intercalation, and the data show no other indication of intercalation. Overall, the experimental data are thus consistent with capacitive charging and surface compensation.

$$C_{dl} = A\frac{\epsilon_0\epsilon}{R}\frac{R+t}{t} \tag{1}$$

The specific areal capacitance (C_A) is then obtained by dividing C_r by the NC surface area. Surprisingly, the C_A values measured here are close to those measured in $Fe^{3+/2+}$:ZnO NCs (33 μF cm^{-2}),[34] where redox activity of the iron dopants provides a substantial boost to the NC capacitance by localizing electrons.

Because the NIR absorption spectra and E_F were both measured simultaneously as a function of $FcBF_4$ titration (Figures 2 and 3), it is possible to recast the data by plotting one measurement vs the other. Figure 4 plots E_F values from Figure 3 against the 1300 nm absorption divided by the absorption of the maximally photodoped NCs at the same wavelength (A/A_{max}), from Figure 2. The dashed lines in Figure 4 show linear fits to the data, not including the data points in the region of the equivalence point (hollow symbols). Extrapolation of these lines to $A/A_{max} = 0$ provides a measure

Table 1. Summary of Nanocrystal Capacitance Results from Figure 3 and Eq 1[a]

Sn^{4+} cation %	mV/equiv.	r(nm)	$A(10^{-16} m^2)$	experimental C_r(aF)	C_{dl} from eq 1 (aF)	experimental $C_A(\mu F\ cm^{-2})$
0	0.71	6.55	5.39	226	313	42
0.85	0.36	6.70	5.64	445	328	79
1.9	0.50	7.05	6.25	302	363	48
3.8	0.47	6.30	4.99	340	290	68

[a] Experimental redox capacitance (C_r) values compared with double-layer capacitance (C_{dl}) values calculated from eq 1 for In_2O_3 NCs with varying amounts of Sn^{4+} doping and t = 1.4 Å. Experimental areal capacitance (C_A) values.

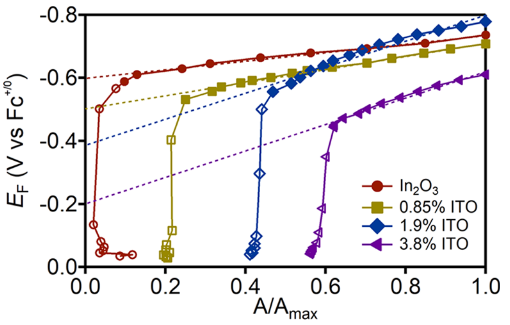

Figure 4. Fermi level (E_F, in V vs $Fc^{+/0}$) of d = 13.1 nm In_2O_3 (red circles), d = 13.4 nm 0.85% ITO (gold squares), d = 14.1 nm 1.9% ITO (blue diamonds), and d = 12.6 nm 3.8% ITO (purple triangles) NCs, plotted against the absorption at 1300 nm, normalized to the maximum absorption of the fully photodoped NCs (A/A_{max}). The dashed lines are linear fits to the data before the equivalence points, extrapolated to E_F at A/A_{max} = 0 to estimate the CB-edge potentials. The hollow symbols are data in the region of the equivalence point and are not included in the analysis. The small upturn in A/A_{max} after titration of the In_2O_3 NCs is due to scattering.

of E_F in the limit of no CB electrons, that is, the CB-edge potential.

Three important potentials are thus obtained from the above data: the maximum E_F after maximal photodoping ($E_{F\ max}$), the value of E_F at A/A_0 = 1 ($E_{F\ as\text{-}made}$), and the CB-edge potential (E_{CB}). These potentials are all plotted as a function of Sn^{4+} concentration for the various ITO NC samples in SI Figure S7. We note that $E_{F\ as\text{-}made}$ varies slightly from sample to sample, attributed to nonsystematic variations in surface stoichiometries, protonation or other ligation levels, and faceting, coming from the independent synthesis and workup steps of each sample; the band-edge potentials of semiconductor NCs are very sensitive to surface dipoles, for example (see SI).[39−42] To factor out these variations, Figure 5a plots $E_{F\ max}$ and E_{CB} relative to $E_{F\ as\text{-}made}$. Figure 5a shows that maximum photodoping always increases E_F by roughly the same amount (118 ± 20 mV), regardless of NC Sn^{4+} concentration. This result is consistent with the observation that $\langle N_{photo} \rangle$ is also independent of Sn^{4+} concentration (SI Figure S5), and with previously observed Fermi-level pinning in photodoped ZnO NCs.[31] Notably, the data in Figure 5a also show that E_{CB} decreases systematically with Sn^{4+} doping, dropping by hundreds of mV going from undoped In_2O_3 to 3.8% $Sn^{4+}:In_2O_3$ NC compositions. These data highlight the conclusion that aliovalent Sn^{4+} dopants *stabilize* the In_2O_3 NC CB edge, rather than raising the Fermi level into the CB as observed during photodoping. An average stabilization energy of ~0.55 mV per lattice Sn^{4+} is estimated from these data, as summarize schematically in Figure 5b. This value corresponds to ~1.20 mV per active lattice Sn^{4+} after accounting for inactive dopants. This type of trend was proposed[4,18] in previous studies of colloidal metal-oxide NC redox reactions but has not previously been measured.

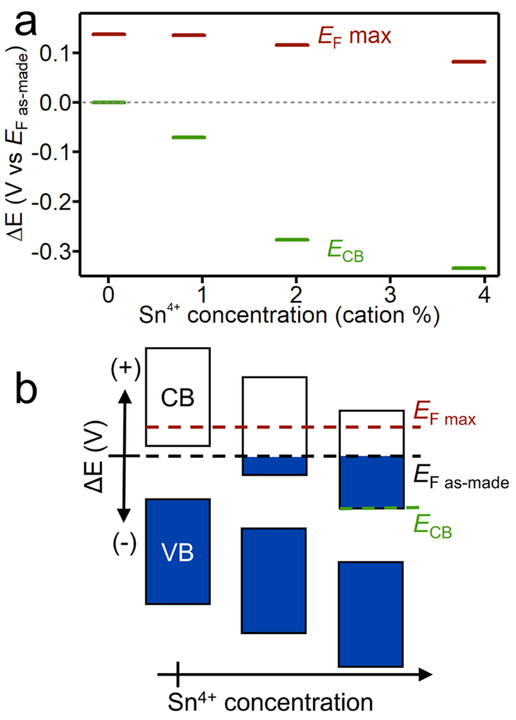

Figure 5. (a) Potentials for In_2O_3 NCs doped with different amounts of Sn^{4+}, plotted relative to the potentials measured at A/A_0 = 1 ($E_{F\ as\text{-}made}$). The red bars indicate the Fermi levels after maximum photodoping ($E_{F\ max}$). The green bars indicate the CB-edge potentials, derived from extrapolation of the titration data in Figure 4 to A/A_{max} = 0, that is, E_F in the limit of $\langle n \rangle$ = 0. (b) Schematic summary of the results in panel (a), showing band-edge stabilization upon Sn^{4+} doping into In_2O_3 NCs.

Modeling the Electrostatics. To shed further light on the experimental trends summarized in Figure 5, we have employed the hybrid quantum-classical "Charged Sphere" model.[33] This model describes the effects of electrostatics on the potentials of band-like charge carriers in NCs, and has previously been used to analyze experimental potentiometric titration data collected for photodoped ZnO and $Fe^{3+/2+}$:ZnO NCs,[33,34] both involving CB electrons stabilized by surface charge-compensating cations. Here, we have expanded the Charged Sphere model to describe electrostatic interactions between band-like charge carriers and aliovalent dopants *within* the NC lattice, focusing on modeling the trend in CB-edge potentials of ITO NCs observed experimentally (Figure 5).

Figure 6 illustrates the electrostatic contributions of CB electrons (q^- = ne), their charge-compensating cations (q^+), and the material's electron affinity (EA) to the Fermi-level (electrochemical) potential ($V(r)$) of degenerately n-doped

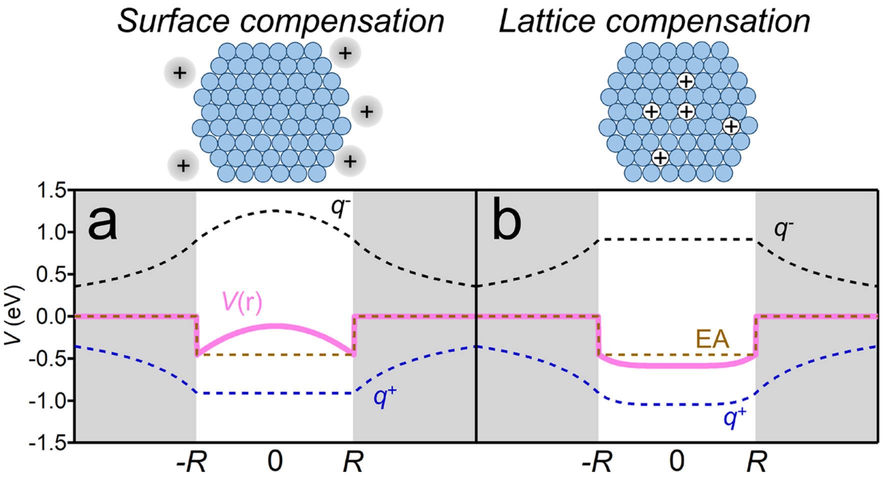

Figure 6. Illustration of electrostatic contributions to the Fermi-level electron potential energies ($V(r)$) for degenerately *n*-doped In_2O_3 NCs in which CB electrons are compensated by either (a) surface (e.g., H^+) or (b) lattice (e.g., Sn^{4+}) cations. For this illustration, potentials calculated using the Charged Sphere model for NC values of $q^- = q^+ = 40$ and $R = 7$ nm are plotted as a function of distance from the NC center ($r = 0$). These values correspond to an active dopant concentration of ∼0.1%, similar to the low-concentration ITO NCs investigated experimentally (∼0.2%). In each plot, the white region represents the NC interior, $r = R$ represents the NC radius (surface), and the shaded regions represent the surrounding dielectric. Electrostatic contributions from CB electrons (q^-, black), charge-compensating cations (q^+, blue), and electron affinity (EA, gold) combine to define the total potential as a function of radius, $V(r)$ (pink). For all calculations, a value of $\epsilon = 9.0$ is used for the dielectric constant of the solvent (0.1 M $TBAPF_6$/THF). The dielectric constant ($\epsilon = 12.5$) and electron affinity (EA = 4.1 eV) are chosen to be the same for In_2O_3 and ITO NCs.

NCs involving either surface (Figure 6a) or lattice (Figure 6b) charge compensation (see SI for computational details). Using $q^- = q^+ = 40$, $R = 7$ nm, and model parameters suitable for In_2O_3 NCs, Figure 6a illustrates how surface charge-compensating cations such as H^+ or electrolyte in capacitive charging experiments minimize $V(r)$ near the NC surfaces, consistent with, for example, experimental findings of constant surface areal capacitance values in H^+-compensated photodoped ZnO NCs of different radii.[32] In contrast, Figure 6b shows that $V(r)$ is lowered in the internal volume of the NC by uniformly distributed aliovalent dopants. This result illustrates the central experimental conclusion presented above that aliovalent dopants *stabilize* NC band-edge potentials relative to an externally determined Fermi level.

To illustrate further, the potential energies of the Fermi-level electrons in $d = 14$ nm In_2O_3 NCs in the one-electron ($q^- = 1$) limit were calculated for various Sn^{4+} doping levels, again assuming uniform dopant distributions. This scenario relates to the band-edge potentials (E_{CB}) described in Figures 4, 5 (deduced from the $q^- = 0$ limit). In the absence of Sn^{4+} dopants, the potential energy is described by a square-well potential (Figure 7). Increasing the Sn^{4+} concentration rapidly lowers the electron's potential energy, consistent with experiment.

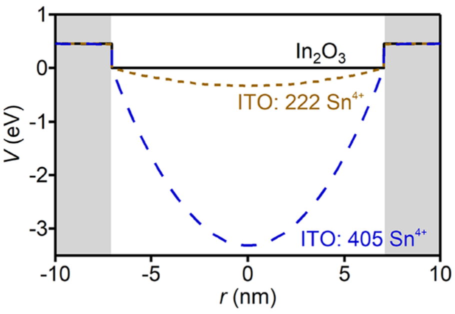

Figure 7. Potential energies calculated using the Charged Sphere model for an $R = 7$ nm In_2O_3 NC containing only one CB electron ($q^- = 1$, to probe the CB-edge potential) and 0 (black), 222 (gold), and 405 (blue) lattice Sn^{4+} (q^+) dopants distributed uniformly throughout the NC volume. The white regions correspond to the NC interior and the gray regions correspond to the surrounding dielectric. For all calculations, a value of 9.0 is used for the dielectric constant of the solvent (0.1 M $TBAPF_6$/THF). The dielectric constant and EA of the ITO NCs are chosen to be the same as for In_2O_3, i.e., $\epsilon = 12.5$ and EA = 4.1 eV. See SI for further details about the model calculations.

Although the ITO NC synthesis used here is expected to yield a uniform distribution of Sn^{4+} dopants,[19,24] the experimental finding that only ∼40% of these dopants are active means the distribution of active dopants is unknown and may itself not be uniform. In other cases, intentional nonuniform aliovalent doping has been used as an effective means of tuning LSPR profiles.[19,43] Relaxing the assumption of uniform active dopant distributions within the NC volume, the Charged Sphere model shows that $V(r)$ is critically dependent on the dopant radial distribution (see SI). If, for example, a radial "active" Sn^{4+} gradient is used that increases the effective doping probability with increasing r, then $V(r)$ flattens even more inside the NC and the overall CB stabilization is smaller than in the case of uniform internal doping (SI Figure S8). Gradients of this type are thus intermediate between the uniform aliovalent doping and surface-compensated capacitive charging scenarios illustrated in Figure 6. We note that the potential energy surfaces in Figures 6, 7, and SI Figure S8 are qualitatively reminiscent of the CB depletion profiles calculated for ITO NCs in ref 26. Whereas that modeling was used to interpret how the NC responds when an applied external field raises or lowers the Fermi level, the modeling here highlights the band-edge stabilization by aliovalent dopants relative to a fixed external Fermi level. Overall, all calculations within the Charged Sphere model show the same trend of CB stabilization by aliovalent dopants, consistent with the key experimental observations reported here.

The results presented above highlight the important role that aliovalent dopants play in defining the band-edge potentials of ITO NCs, and by extension, of aliovalently doped semiconductor NCs in general. Quantitative redox titrations show that only ~40% of Sn^{4+} dopants actively stabilize excess CB electrons in these NCs, similar to previous findings for AZO NCs.[16] Spectroelectrochemical data show that the active aliovalent dopants in ITO NCs stabilize the CB edge by ~1.20 mV per Sn^{4+} (or ~0.55 mV per total Sn^{4+}) on average. Calculations using the Charged Sphere model illustrate the potential energy surfaces that result from aliovalent doping, highlighting their differences from those resulting from photodoping, and emphasize the sensitivity of $V(r)$ to active dopant radial profiles.

The spectroelectrochemical titration data highlight the reactivity difference between CB electrons added via aliovalent doping (CB stabilization) and via photodoping (Fermi level raising): all $e^-_{\mathrm{CB,\,photo}}$ can be removed by the mild oxidant $FcBF_4$, but only ~30% of $e^-_{\mathrm{CB,\,alio}}$ can be removed using the same oxidant. Similar reactivity trends have been observed in other aliovalently doped oxide NCs,[16,18] but without knowledge of the associated potentials. This reactivity difference reflects the importance of the carrier's specific charge-compensating motif. In the case of $e^-_{\mathrm{CB,\,photo}}$, charge-compensating surface protons can assist in discharging the NC through proton-coupled electron transfer (PCET), or can assist merely by providing less stabilization of $e^-_{\mathrm{CB,\,photo}}$ because of their spatial separation from the charge carriers. Removal of $e^-_{\mathrm{CB,\,alio}}$ is thermodynamically more costly because it requires greater net charge separation.[16]

The CB stabilization energy by aliovalent dopants in ITO NCs is similar to that found in *p*-doped d = 5.4 nm $Cu_{2-x}S$ NCs.[35] Here, Cu^+ vacancies, which play the same electrostatic role as aliovalent dopants, were estimated experimentally to stabilize VB holes by ~2.3 mV/vacancy (determined at a hole density of ~1.5×10^{21} cm^{-3}). The similar stabilization per charged dopant/defect despite the different NC structure, composition, and excess charge-carrier type supports generalization of the conclusion that aliovalent doping shifts NC band edges relative to the surrounding environment, ultimately permitting accumulation of excess band-like carriers.

Finally, the capacitance values measured in these In_2O_3-based NCs (C_r = 226−445 aF) are surprisingly large compared to values measured for analogous ZnO NCs (C_r = 2−12 aF) and are even large compared to $Fe^{3+/2+}$:ZnO NCs (C_r = 45−80 aF).[32,34] Even Sn^{4+}-free In_2O_3 NCs show a very large capacitance (C_r = 226 aF), so this difference cannot be associated with the added tin. We note that the In_2O_3 NCs studied here are substantially larger than the previously studied ZnO and $Fe^{3+/2+}$:ZnO NCs (d = 12−15 nm vs 4.5−9.3 nm); previous experimental work has demonstrated an increase in ZnO NC capacitance with increasing NC size.[32] The Charged Sphere model also predicts that, compared to small NCs, larger NCs experience smaller changes to their Fermi level when the electrical double layer is perturbed or when the number of CB electrons changes,[33] translating to a larger capacitance (see SI). If all other factors were equal, these capacitance differences would be accounted for by normalizing to NC surface area, as found for ZnO NCs,[32] but Table 1 shows that C_A values for these In_2O_3-based NCs are also much larger than those of the ZnO-based NCs (C_A = 42−79 μF cm^{-2} vs 4−33 μF cm^{-2}). In the idealized double-layer capacitance model of eq 1, this capacitance difference would imply a larger t for ZnO than for In_2O_3 NCs, but it likely has a more significant origin. Instead, this large capacitance difference is tentatively attributed to a greater intrinsic density of states (DOS) near the CB edge in In_2O_3 NCs compared to ZnO NCs, consistent with, for example, the larger maximum electron densities achievable in In_2O_3 and ITO[18,19] NCs compared to ZnO[27] and AZO[16,17] NCs. Such large capacitance values in colloidal NCs could prove attractive for reversible charge-storage applications, for example, in NC-based redox flow batteries.

CONCLUSION

Charge compensation of CB electrons in degenerately *n*-doped oxide NCs has been examined by spectroelectrochemistry combined with photodoping and redox titrations. Using ITO NCs as a model system, the potentials of CB electrons added via photodoping and via aliovalent doping were measured. A marked difference is observed between the electrochemical potentials of CB electrons compensated by aliovalent dopants (Sn^{4+}) and those compensated by surface cations (e.g., H^+); the CB is dramatically stabilized by incorporation of Sn^{4+} dopants into the In_2O_3 NC lattice. Theoretical modeling supports a description in which aliovalent dopants stabilize the CB-edge, in contrast with photodoping, which raises the solution electrochemical potential. The insights from these results are anticipated to translate to other aliovalently doped NCs, and will help to inform the use of such charge-tunable degenerately doped semiconductor NCs in sensing, plasmonics, charge-controlled magnetism, or energy applications.

METHODS

Materials. Unless otherwise noted, all materials were used as received without further purification. Anhydrous tetrahydrofuran (THF) was purified through columns of dried alumina. Oleic acid (OA, technical grade) and tetrachloroethylene were purchased from Sigma-Aldrich. Indium(III) acetate (99.99%) and oleyl alcohol (tech., 80−85%) were purchased from Alfa Aesar. Tin(IV) acetate was purchased from Fisher Scientific. Ferrocenium tetrafluoroborate ($FcBF_4$) was prepared from ferrocene and HBF_4OEt_2 (Sigma-Aldrich) following literature procedures.[44] Tetrabutylammonium hexafluorophosphate ($TBAPF_6$, 98%, Sigma-Aldrich) was recrystallized three times from absolute ethanol, then dried under vacuum for 48 h at 120 °C before anaerobically transferring into a N_2 glovebox.

ITO Nanocrystal Synthesis. In_2O_3 and ITO NCs were synthesized according to previously published procedures.[19,24] Briefly, 7.5 mmol of metal acetate were added to a 100 mL three-neck flask along with 15 mL of OA. Tin doping was achieved by holding the total metal content at 7.5 mmol and adjusting the ration of Sn:In. The solution was then heated with stirring under N_2 with a purge needle for at least 2 h to obtain a 0.5 mmol/mL solution. Thirteen mL of oleyl alcohol were added to a separate 100 mL three-neck flask that was fitted with three septa. Three 16-gauge needles were added to one side, and a 16-gauge needle was added to the other side with a N_2 flow of 130 cc/min. The flask was then heated to 290 °C. Next, 10 mL of the ITO precursor solution was injected using a glass syringe and syringe pump at a rate of 0.35 mL/min. The flask was then allowed to cool to room temperature, and the NCs were collected by precipitation with EtOH and centrifugation. The product was then suspended in toluene and precipitated with EtOH. This washing procedure was repeated three more times. Finally, the NCs were dispersed in hexanes and filtered with a 0.2 μm PTFE syringe filter. The solvent was then evaporated, and the product pumped into a N_2 glovebox. The NCs were dispersed in anhydrous THF for further analysis.

Physical Measurements. All UV−vis-NIR absorption spectra were collected at room temperature using a Cary 5000 spectrophotometer (Agilent) and fiber-optic coupling into a N_2 glovebox.

Transmission electron microscope (TEM) images were taken on a FEI Tecnai G2 F20 operating at 200 kV. Average NC sizes were obtained from statistical analysis of at least 100 NCs measured from TEM images. See SI Figure S1 for further details. NC concentrations were determined using a combination of TEM and inductively coupled plasma atomic emission spectroscopy (ICP-AES, PerkinElmer) of dried NCs digested in ultrapure nitric acid.

Photodoping and Spectroelectrochemistry. All electrochemical measurements were performed in a N_2 glovebox with a Gamry potentiostat under galvanostatic control with $I = 0$ A. Two Pt wires were used for the working and counter electrode, and a 1 mm leakless Ag/AgCl electrode (eDAQ) was used as a reference. The electrodes were fitted through the septum of a GL-14 cap and secured on a 1 cm quartz cuvette (Starna Cells) containing 3.5 mL of 0.1 M $TBAPF_6$/THF, 10 μL of anhydrous EtOH, and 15−50 μL of NC solution. The solution was magnetically stirred during the experiment. The absorption spectrum was collected and the open-circuit potential (V_{OC}) was allowed to equilibrate, then the solution was irradiated with a 340 nm LED to allow the NCs to maximally photodope. Because of small excitation rates, maximum photodoping required several hours (5−8 h) illumination under these conditions. $FcBF_4$ was dissolved in 0.1 M $TBAPF_6$/THF and this solution was further diluted in fresh 0.1 M $TBAPF_6$/THF such that 5 μL of the dilute solution contained 15−35 equiv of Fc^+ per NC. After allowing the NCs to maximally photodope, the absorption spectrum was measured, and then an aliquot of $FcBF_4$ was injected through the septum. The V_{OC} was allowed to equilibrate, and the absorption spectrum was measured again. Potentials and absorption data were thus measured simultaneously. This injection/equilibration/measurement cycle was repeated until a large excess of $FcBF_4$ had been added, as judged from V_{OC}. All potentials were referenced to the $E_{1/2}$ of $Fc^{+/0}$ measured by cyclic voltammetry following the potentiometry measurements.

Theoretical Modeling. The quantum-classical Charged Sphere model[33,34] was adapted to simulate the Fermi levels of aliovalently doped NCs. The effects of multiple CB electrons and uncompensated aliovalent dopants are approximated as a mean-field potential ($V(r)$) in the Hamiltonian, as described by eq 2.

$$\hat{H} = -\frac{1}{2}\frac{d^2}{dr^2} + \frac{l(l+1)}{2r^2} + V(r) \tag{2}$$

The mean-field potential can be derived from Gauss's law using eq 3 and 4, as described previously,[33,34] where $\rho(r)$ is used to represent the radial density distributions of CB electrons and uncompensated cations. Further details including about calculation of Fermi levels are provided in the SI.

$$\mathrm{V(r)} = \int_{\infty}^{r} E(r')dr' \tag{3}$$

$$E(r) = \frac{\iiint \rho(r)dV}{\epsilon(r)r^2} \tag{4}$$

ASSOCIATED CONTENT

Supporting Information

The Supporting Information is available free of charge at https://pubs.acs.org/doi/10.1021/acsnano.1c04660.

> Size analysis, absorption, and titration data for In_2O_3 and ITO NCs of varying Sn^{4+} concentration, potentiometric titration data, description of computational methods, and charged sphere model calculations (PDF)

AUTHOR INFORMATION

Corresponding Author

Daniel R. Gamelin − *Department of Chemistry, University of Washington, Seattle, Washington 98195-1700, United States;* orcid.org/0000-0003-2888-9916; Email: gamelin@uw.edu

Authors

Jose J. Araujo − *Department of Chemistry, University of Washington, Seattle, Washington 98195-1700, United States;* orcid.org/0000-0003-0955-2584

Carl K. Brozek − *Department of Chemistry, University of Washington, Seattle, Washington 98195-1700, United States;* Present Address: (C.K.B.) Department of Chemistry and Biochemistry, University of Oregon, Eugene, Oregon 97403, United States*;* orcid.org/0000-0002-8014-7904

Hongbin Liu − *Department of Chemistry, University of Washington, Seattle, Washington 98195-1700, United States;* Present Address: (H.L.) Microsoft Quantum, Redmond, Washington 98052, United States.*;* orcid.org/0000-0001-9011-1182

Anna Merkulova − *Department of Chemistry, University of Washington, Seattle, Washington 98195-1700, United States*

Xiaosong Li − *Department of Chemistry, University of Washington, Seattle, Washington 98195-1700, United States;* orcid.org/0000-0001-7341-6240

Complete contact information is available at: https://pubs.acs.org/10.1021/acsnano.1c04660

Notes

The authors declare no competing financial interest.

ACKNOWLEDGMENTS

This work was primarily supported by the U.S. National Science Foundation through the UW Molecular Engineering Materials Center (MEM-C), a Materials Research Science and Engineering Center (DMR-1719797). Valuable support through CHE-1904436 (to D.R.G.) and CHE-1856210 (to X.L.) is gratefully acknowledged. Part of this work was conducted at the Molecular Analysis Facility, a National Nanotechnology Coordinated Infrastructure (NNCI) site at the University of Washington that is supported in part by the National Science Foundation (2025489 and 154210), the University of Washington, the Molecular Engineering & Sciences Institute, the Clean Energy Institute, and the National Institutes of Health.

REFERENCES

(1) Agrawal, A.; Cho, S. H.; Zandi, O.; Ghosh, S.; Johns, R. W.; Milliron, D. J. Localized Surface Plasmon Resonance in Semiconductor Nanocrystals. *Chem. Rev.* **2018**, *118*, 3121−3207.

(2) Kriegel, I.; Scotognella, F.; Manna, L. Plasmonic Doped Semiconductor Nanocrystals: Properties, Fabrication, Applications and Perspectives. *Phys. Rep.* **2017**, *674*, 1−52.

(3) Luther, J. M.; Jain, P. K.; Ewers, T.; Alivisatos, A. P. Localized Surface Plasmon Resonances Arising from Free Carriers in Doped Quantum Dots. *Nat. Mater.* **2011**, *10*, 361−366.

(4) Schimpf, A. M.; Knowles, K. E.; Carroll, G. M.; Gamelin, D. R. Electronic Doping and Redox-Potential Tuning in Colloidal Semiconductor Nanocrystals. *Acc. Chem. Res.* **2015**, *48*, 1929−1937.

(5) Liu, W. K.; Whitaker, K. M.; Smith, A. L.; Kittilstved, K. R.; Robinson, B. H.; Gamelin, D. R. Room-Temperature Electron Spin Dynamics in Free-Standing ZnO Quantum Dots. *Phys. Rev. Lett.* **2007**, *98*, 186804.

(6) Ochsenbein, S. T.; Feng, Y.; Whitaker, K. M.; Badaeva, E.; Liu, W. K.; Li, X.; Gamelin, D. R. Charge-Controlled Magnetism in Colloidal Doped Semiconductor Nanocrystals. *Nat. Nanotechnol.* **2009**, *4*, 681−687.

(7) Staller, C. M.; Gibbs, S. L.; Saez Cabezas, C. A.; Milliron, D. J. Quantitative Analysis of Extinction Coefficients of Tin-Doped Indium Oxide Nanocrystal Ensembles. *Nano Lett.* **2019**, *19*, 8149−8154.

(8) Hartstein, K. H.; Schimpf, A. M.; Salvador, M.; Gamelin, D. R. Cyclotron Splittings in the Plasmon Resonances of Electronically Doped Semiconductor Nanocrystals Probed by Magnetic Circular Dichroism Spectroscopy. *J. Phys. Chem. Lett.* **2017**, *8*, 1831−1836.

(9) Yin, P.; Tan, Y.; Fang, H.; Hegde, M.; Radovanovic, P. V. Plasmon-Induced Carrier Polarization in Semiconductor Nanocrystals. *Nat. Nanotechnol.* **2018**, *13*, 463−467.

(10) Araujo, J. J.; Brozek, C. K.; Kroupa, D. M.; Gamelin, D. R. Degenerately *n*-Doped Colloidal PbSe Quantum Dots: Band Assignments and Electrostatic Effects. *Nano Lett.* **2018**, *18*, 3893−3900.

(11) Ghini, M.; Curreli, N.; Camellini, A.; Wang, M.; Asaithambi, A.; Kriegel, I. Photodoping of Metal Oxide Nanocrystals for Multi-Charge Accumulation and Light-Driven Energy Storage. *Nanoscale* **2021**, *13*, 8773−8783.

(12) Shim, M.; Guyot-Sionnest, P. *n*-Type Colloidal Semiconductor Nanocrystals. *Nature* **2000**, *407*, 981−983.

(13) Shim, M.; Wang, C.; Guyot-Sionnest, P. Charge-Tunable Optical Properties in Colloidal Semiconductor Nanocrystals. *J. Phys. Chem. B* **2001**, *105*, 2369−2373.

(14) Wang, C.; Shim, M.; Guyot-Sionnest, P. Electrochromic Nanocrystal Quantum Dots. *Science* **2001**, *291*, 2390−2392.

(15) Wehrenberg, B. L.; Guyot-Sionnest, P. Electron and Hole Injection in PbSe Quantum Dot Films. *J. Am. Chem. Soc.* **2003**, *125*, 7806−7807.

(16) Schimpf, A. M.; Ochsenbein, S. T.; Buonsanti, R.; Milliron, D. J.; Gamelin, D. R. Comparison of Extra Electrons in Colloidal *n*-Type Al^{3+}-Doped and Photochemically Reduced ZnO Nanocrystals. *Chem. Commun.* **2012**, *48*, 9352−9354.

(17) Zhou, D.; Wang, P.; Roy, C. R.; Barnes, M. D.; Kittilstved, K. R. Direct Evidence of Surface Charges in *n*-Type Al-Doped ZnO. *J. Phys. Chem. C* **2018**, *122*, 18596−18602.

(18) Schimpf, A. M.; Lounis, S. D.; Runnerstrom, E. L.; Milliron, D. J.; Gamelin, D. R. Redox Chemistries and Plasmon Energies of Photodoped In_2O_3 and Sn-Doped In_2O_3 (ITO) Nanocrystals. *J. Am. Chem. Soc.* **2015**, *137*, 518−524.

(19) Crockett, B. M.; Jansons, A. W.; Koskela, K. M.; Johnson, D. W.; Hutchison, J. E. Radial Dopant Placement for Tuning Plasmonic Properties in Metal Oxide Nanocrystals. *ACS Nano* **2017**, *11*, 7719−7728.

(20) Crockett, B. M.; Jansons, A. W.; Koskela, K. M.; Sharps, M. C.; Johnson, D. W.; Hutchison, J. E. Influence of Nanocrystal Size on the Optoelectronic Properties of Thin, Solution-Cast Sn-Doped In_2O_3 Films. *Chem. Mater.* **2019**, *31*, 3370−3380.

(21) Gordon, T. R.; Paik, T.; Klein, D. R.; Naik, G. V.; Caglayan, H.; Boltasseva, A.; Murray, C. B. Shape-Dependent Plasmonic Response and Directed Self-Assembly in a New Semiconductor Building Block, Indium-Doped Cadmium Oxide (ICO). *Nano Lett.* **2013**, *13*, 2857−2863.

(22) Kriegel, I.; Urso, C.; Viola, D.; De Trizio, L.; Scotognella, F.; Cerullo, G.; Manna, L. Ultrafast Photodoping and Plasmon Dynamics in Fluorine-Indium Codoped Cadmium Oxide Nanocrystals for All-Optical Signal Manipulation at Optical Communication Wavelengths. *J. Phys. Chem. Lett.* **2016**, *7*, 3873−3881.

(23) Runnerstrom, E. L.; Llordes, A.; Lounis, S. D.; Milliron, D. J. Nanostructured Electrochromic Smart Windows: Traditional Materials and NIR-Selective Plasmonic Nanocrystals. *Chem. Commun.* **2014**, *50*, 10555−10572.

(24) Jansons, A. W.; Hutchison, J. E. Continuous Growth of Metal Oxide Nanocrystals: Enhanced Control of Nanocrystal Size and Radial Dopant Distribution. *ACS Nano* **2016**, *10*, 6942−6951.

(25) Agrawal, A.; Kriegel, I.; Runnerstrom, E. L.; Scotognella, F.; Llordes, A.; Milliron, D. J. Rationalizing the Impact of Surface Depletion on Electrochemical Modulation of Plasmon Resonance Absorption in Metal Oxide Nanocrystals. *ACS Photonics* **2018**, *5*, 2044−2050.

(26) Zandi, O.; Agrawal, A.; Shearer, A. B.; Reimnitz, L. C.; Dahlman, C. J.; Staller, C. M.; Milliron, D. J. Impacts of Surface Depletion on the Plasmonic Properties of Doped Semiconductor Nanocrystals. *Nat. Mater.* **2018**, *17*, 710−717.

(27) Schimpf, A. M.; Gunthardt, C. E.; Rinehart, J. D.; Mayer, J. M.; Gamelin, D. R. Controlling Carrier Densities in Photochemically Reduced Colloidal ZnO Nanocrystals: Size Dependence and Role of the Hole Quencher. *J. Am. Chem. Soc.* **2013**, *135*, 16569−16577.

(28) Valdez, C. N.; Braten, M.; Soria, A.; Gamelin, D. R.; Mayer, J. M. Effect of Protons on the Redox Chemistry of Colloidal Zinc Oxide Nanocrystals. *J. Am. Chem. Soc.* **2013**, *135*, 8492−8495.

(29) Valdez, C. N.; Delley, M. F.; Mayer, J. M. Cation Effects on the Reduction of Colloidal ZnO Nanocrystals. *J. Am. Chem. Soc.* **2018**, *140*, 8924−8933.

(30) Valdez, C. N.; Schimpf, A. M.; Gamelin, D. R.; Mayer, J. M. Proton-Controlled Reduction of ZnO Nanocrystals: Effects of Molecular Reductants, Cations, and Thermodynamic Limitations. *J. Am. Chem. Soc.* **2016**, *138*, 1377−1385.

(31) Carroll, G. M.; Schimpf, A. M.; Tsui, E. Y.; Gamelin, D. R. Redox Potentials of Colloidal *n*-Type ZnO Nanocrystals: Effects of Confinement, Electron Density, and Fermi-Level Pinning by Aldehyde Hydrogenation. *J. Am. Chem. Soc.* **2015**, *137*, 11163−11169.

(32) Brozek, C. K.; Hartstein, K. H.; Gamelin, D. R. Potentiometric Titrations for Measuring the Capacitance of Colloidal Photodoped ZnO Nanocrystals. *J. Am. Chem. Soc.* **2016**, *138*, 10605−10610.

(33) Liu, H.; Brozek, C. K.; Sun, S.; Lingerfelt, D. B.; Gamelin, D. R.; Li, X. A Hybrid Quantum-Classical Model of Electrostatics in Multiply Charged Quantum Dots. *J. Phys. Chem. C* **2017**, *121*, 26086−26095.

(34) Brozek, C. K.; Zhou, D.; Liu, H.; Li, X.; Kittilstved, K. R.; Gamelin, D. R. Soluble Supercapacitors: Large and Reversible Charge Storage in Colloidal Iron-Doped ZnO Nanocrystals. *Nano Lett.* **2018**, *18*, 3297−3302.

(35) Hartstein, K. H.; Brozek, C. K.; Hinterding, S. O. M.; Gamelin, D. R. Copper-Coupled Electron Transfer in Colloidal Plasmonic Copper-Sulfide Nanocrystals Probed by *in Situ* Spectroelectrochemistry. *J. Am. Chem. Soc.* **2018**, *140*, 3434−3442.

(36) Goings, J. J.; Schimpf, A. M.; May, J. W.; Johns, R. W.; Gamelin, D. R.; Li, X. Theoretical Characterization of Conduction-Band Electrons in Photodoped and Aluminum-Doped Zinc Oxide (AZO) Quantum Dots. *J. Phys. Chem. C* **2014**, *118*, 26584−26590.

(37) Farvid, S. S.; Hegde, M.; Radovanovic, P. V. Influence of the Host Lattice Electronic Structure on Dilute Magnetic Interactions in Polymorphic Cr(III)-Doped In_2O_3 Nanocrystals. *Chem. Mater.* **2013**, *25*, 233−244.

(38) Farvid, S. S.; Ju, L.; Worden, M.; Radovanovic, P. V. Colloidal Chromium-Doped In_2O_3 Nanocrystals as Building Blocks for High-T_C Ferromagnetic Transparent Conducting Oxide Structures. *J. Phys. Chem. C* **2008**, *112*, 17755−17759.

(39) Brown, P. R.; Kim, D.; Lunt, R. R.; Zhao, N.; Bawendi, M. G.; Grossman, J. C.; Bulovic, V. Energy Level Modification in Lead Sulfide Quantum Dot Thin Films through Ligand Exchange. *ACS Nano* **2014**, *8*, 5863−5872.

(40) Carroll, G. M.; Tsui, E. Y.; Brozek, C. K.; Gamelin, D. R. Spectroelectrochemical Measurement of Surface Electrostatic Contributions to Colloidal CdSe Nanocrystal Redox Potentials. *Chem. Mater.* **2016**, *28*, 7912−7918.

(41) Kroupa, D. M.; Voros, M.; Brawand, N. P.; McNichols, B. W.; Miller, E. M.; Gu, J.; Nozik, A. J.; Sellinger, A.; Galli, G.; Beard, M. C. Tuning Colloidal Quantum Dot Band Edge Positions Through Solution-Phase Surface Chemistry Modification. *Nat. Commun.* **2017**, *8*, 15257.

(42) Jeong, K. S.; Deng, Z.; Keuleyan, S.; Liu, H.; Guyot-Sionnest, P. Air-Stable *n*-Doped Colloidal HgS Quantum Dots. *J. Phys. Chem. Lett.* **2014**, *5*, 1139−1143.

(43) Staller, C. M.; Robinson, Z. L.; Agrawal, A.; Gibbs, S. L.; Greenberg, B. L.; Lounis, S. D.; Kortshagen, U. R.; Milliron, D. J. Tuning Nanocrystal Surface Depletion by Controlling Dopant

Distribution as a Route toward Enhanced Film Conductivity. *Nano Lett.* **2018**, *18*, 2870−2878.

(44) Connelly, N. G.; Geiger, W. E. Chemical Redox Agents for Organometallic Chemistry. *Chem. Rev.* **1996**, *96*, 877−910.

https://doi.org/10.1021/acsnano.1c04660
ACS Nano 2021, 15, 14116−14124